

PAPER

Strain engineering of core–shell silicon carbide nanowires for mechanical and piezoresistive characterizations

To cite this article: Shinya Nakata *et al* 2019 *Nanotechnology* **30** 265702

View the [article online](#) for updates and enhancements.



IOP | ebooks™

Bringing you innovative digital publishing with leading voices to create your essential collection of books in STEM research.

Start exploring the collection - download the first chapter of every title for free.

Strain engineering of core–shell silicon carbide nanowires for mechanical and piezoresistive characterizations

Shinya Nakata¹, Akio Uesugi¹ , Koji Sugano¹, Francesca Rossi²,
Giancarlo Salviati², Alois Lugstein³  and Yoshitada Isono¹ 

¹ Department of Mechanical Engineering, Kobe University, 1-1 Rokkodai-cho, Nada-ku, Kobe 657-8501, Japan

² IMEM-CNR Institute, Parco Area delle Scienze 37/A, 43124 Parma, Italy

³ Institute of Solid State Electronics, TU Wien, Floragasse 7, A-1040 Vienna, Austria

E-mail: isono@mech.kobe-u.ac.jp

Received 20 December 2018, revised 22 February 2019

Accepted for publication 6 March 2019

Published 9 April 2019



Abstract

This study evaluated the mechanical properties and piezoresistivity of core–shell silicon carbide nanowires (C/S-SiCNWs) synthesized by a vapor–liquid–solid technique, which are a promising material for harsh environmental micro electromechanical systems (MEMS) applications. The C/S-SiCNWs were composed of a crystalline cubic (3C) SiC core wrapped by an amorphous silicon dioxide (SiO_x) shell; however, TEM observations of the NWs showed that hexagonal polytypes (2H, 4H, and 6H) were partially induced in the core by a stacking fault owing to a Shockley partial dislocation. The stress–strain relationship of the C/S-SiCNWs and SiC cores without an SiO_x shell was examined using MEMS-based nanotensile tests. The tensile strengths of the C/S-SiCNWs and SiC cores were 7.0 GPa and 22.4 GPa on average, respectively. The lower strength of the C/S-SiCNWs could be attributed to the SiO_x shell with the surface roughness as the breaking point. The Young's modulus of the C/S-SiCNWs was 247.2 GPa on average, whereas that of the SiC cores had a large value with scatter data ranging from 450 to 580 GPa. The geometrical model of the SiC core based on the transmission electron microscopy observations rationalized this scatter data by the volume content of the stacking fault in the core. The piezoresistive effects of the C/S-SiCNW and SiC core were also evaluated from the *I*–*V* characteristics under uniaxial tensile strain. The gauge factor of -30.7 at 0.008ε for the C/S-SiCNW was approximately two-times larger than that of -15.8 at 0.01ε for the SiC core. This could be caused by an increase of the surface state density at the SiO_x/SiC interface owing to the positive fixed oxide charge of the SiO_x shell.

Keywords: strain engineering, silicon carbide, nanowire, core–shell, gauge factor, MEMS

(Some figures may appear in colour only in the online journal)

1. Introduction

Silicon carbide (SiC) has been recognized as a reliable material for power semiconductors and high-speed and high-temperature electric devices because of its wide bandgap, high breakdown electric field, high saturation velocity, and excellent temperature stability. In addition, SiC is a promising material used as a piezoresistive element for harsh environmental micro

electromechanical systems (MEMSs) operating at elevated temperatures because it shows minimal current leakage even at temperatures above 200 °C, presenting a different result than that of Si. For example, the gauge factors for n-type SiC of cubic (3C) crystal structure and hexagonal (2H, 4H, and 6H) polytypes have shown a constant value in the range of -2 to -30 at temperatures up to 450 °C [1–6], while those of Si piezoresistive elements with a pn junction isolation type decrease

with an increase of the temperature above 200 °C owing to the junction leakage current [7]. The excellent mechanical properties of SiC at elevated temperatures also make it an effective structural material for harsh environmental MEMS [8]. Thus, SiC is increasingly used in force and temperature monitoring technologies at elevated temperatures in various industries, such as automobile, heat engine, thermal power generator, etc. However, the mechanical and electrical characteristics for clarifying the piezoresistivity of SiC have been mainly studied for two-dimensional thin films deposited by chemical vapor deposition (CVD) [9, 10].

One-dimensional silicon-related semi-conductive nanowires, such as Si nanowires (SiNWs), SiC nanowires (SiCNWs), etc, are attractive as a force sensing element having a high piezoresistive effect, which is attributed to the drastic changes in the electronic structural features and/or the modification of the surface charge redistribution owing to external stresses [11, 12]. Most of studies on the high piezoresistivity of semi-conductive nanowires were inspired by the report from He *et al* [11], where they demonstrated that the piezoresistance coefficient of the vapor–liquid–solid (VLS)-grown p-doped $\langle 111 \rangle$ SiNWs was 35 times larger than that of bulk Si in a small strain range. Their high piezoresistivity experimental result was also supported through the first-principle calculations by Cao *et al* for the $\langle 111 \rangle$ SiNW model without termination atoms [13], although the dangling bonds on the wire wall generally react with oxygen and hydroxide in practical use. Lugstein *et al* [14, 15] studied the electron mobility and piezoresistivity for VLS-grown SiNWs, and they argued that the high piezoresistivity of the SiNWs was determined by the filling or depopulation of the surface states based on the stress-induced modulation of the surface potential. The high piezoresistivity of the SiNWs was a result of the stress-induced carrier mobility change by controlling the nature and density of the surface states. As described, there are many experimental findings on the piezoresistivity of SiNWs for force sensor applications with a high sensitivity.

Conversely, there are minimal studies on the piezoresistivity of SiCNWs because most of the studies on SiCNWs have been focused on their epitaxial growth [16–19]. Gao *et al* experimentally investigated the piezoresistivity of p-type 6H-SiCNWs using an atomic force microscopy [20] and showed that the resistivity of the 6H-SiCNWs decreased with an increase of the force. Their experiments showed the opposite phenomena to those of p-type semi-conductors, although this could be caused by the multiaxial stress distribution. Shao *et al* carried out *in situ* transmission electron microscopy (TEM) tensile testing for $\langle 111 \rangle$ oriented 3C-SiCNWs [21]; however, the gauge factor of the 3C-SiCNWs was -6.9 , which was equal to half of the factor for the n-type $\langle 100 \rangle$ oriented 3C-SiC films with a thickness of 2 μm prepared by CVD techniques [22]. A few experimental data on the piezoresistivity of SiCNWs have hindered a reliable design of harsh environmental MEMS using the SiCNWs. Thus, a quantitative and a precise evaluation of the mechanical and electrical properties of SiCNWs are important for their application as force-sensors utilized at elevated temperatures.

This study experimentally evaluated the mechanical properties and piezoresistivity of VLS-grown core–shell SiCNWs (C/S-SiCNWs) using a nanotensile testing MEMS device [23–27]. The C/S-SiCNWs have been developed by Salviati *et al* [28, 29], and they are formed by a 3C crystalline core of SiC wrapped by an amorphous SiO_x layer. This study evaluated the crystalline SiC core by TEM observations and the stress–strain relationship, elastic properties, and I – V characteristics of uniaxial strained C/S-SiCNWs and SiC cores. Similar to the SiNW study previously discussed, this study also considered the effect of the surface states via the SiO_x shell on the carrier mobility in the C/S-SiCNW experiments.

2. Experimental procedures

2.1. VLS synthesis of the core–shell SiCNWs

The C/S-SiCNWs were grown on an Si substrate with a $\{100\}$ plane by an iron-assisted carbothermal method based on a VLS mechanism [28]. The growth was performed at atmospheric pressure in a CVD open tube system, depositing ferric nitrate ($\text{Fe}(\text{NO}_3)_3$) as a catalyst and flowing CO ($4 \times 10^{-6} \text{ m}^3 \text{ s}^{-1}$) as a gaseous precursor at 1100 °C for 30 min. The catalysts were dissolved in ethanol, and a non-ionic surfactant was added to enhance ethanol wetting of the silicon. First, the Si substrate was rinsed in an ultrasonic bath with an organic solvent, and then it was etched in a HF solution to remove the SiO_2 layer on the substrate. After rinsing and drying the substrate, the catalyst solution was dropped onto the substrate.

The C/S-SiCNWs grew as curly hair in the CVD chamber. In the growth process, any Si-related gaseous species, such as SiH_4 , SiCl_4 , and SiH_2Cl_2 , etc, were not supplied to the chamber. Only CO and N_2 were supplied as the precursor and purge gases, respectively. A precursor of Si for the SiCNWs was supplied from the substrate. In particular, gaseous SiO species were released from the substrate. Consequently, the following reaction would occur on the catalysts.



This study examined the morphological characteristics of the C/S-SiCNWs using TEM (JEOL 2100F) after the VLS growth.

2.2. Configuration of the electrostatically actuated nanotensile testing device

This study developed an electrostatically actuated nanotensile testing device (EANAT). Although MEMS-based nanotensile testing devices have been developed for the evaluation of the mechanical and electrical properties of silicon and carbon related nanowires [21–27], these devices have been employed for approximately 100 nm diametric nanowires. In order to guarantee the experimental stability associated with a safe treatment of nanowires with a diameter less than 50 nm and to achieve fine resolutions in the load and displacement measurements, more

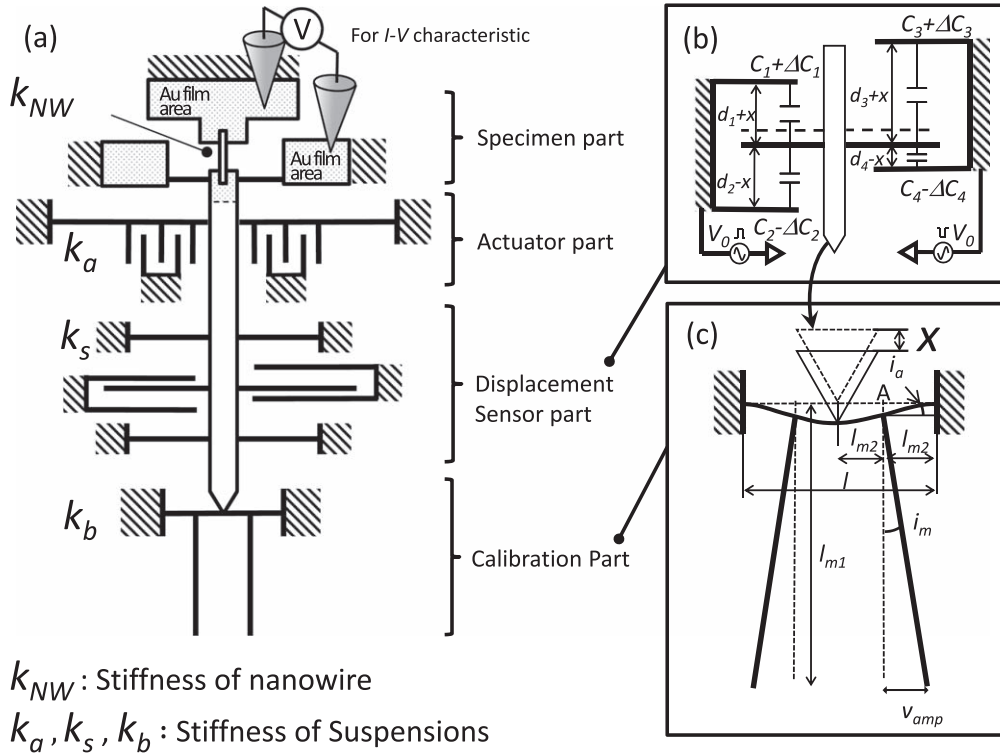


Figure 1. Schematic of the EANAT device: (a) configuration of the functional elements on the EANAT, (b) schematic of the differential displacement sensor with 36 pairs of parallel plates and a 2 μm gap between the plates, and (c) schematic of the calibration part with a geometric amplification system. The moving distance at the free end of the cantilever beam in the system from its initial position is 19.97 times the moving distance of the actuator, depending on the geometrical condition.

miniaturized devices are required. Figure 1(a) schematically shows the configuration of the newly designed EANAT, including four functional parts: the specimen, electrostatically driven actuator, differential capacitive displacement sensor, and calibration parts. The specimen part had gold (Au) film electrodes for I - V characterization of nanowire bridging at the gap of the part. In the differential capacitive sensor (see figure 1(b)), 36 pairs of parallel plates with a 2 μm gap distance were employed. The scale factor of the sensor was 0.177 fF nm^{-1} in the device design, and the output voltage was derived from the charge amplifier circuit (AT1006, ACT-LSI Inc.) connected to the sensor.

The calibration part was composed of a doubly-clamped beam with two long-cantilevers symmetrically placed on the beam for a geometric amplification system, as shown in figure 1(c). This system was able to mechanically amplify the actuator displacement, which was proposed in a previous study [25]. The geometric function of the system showed good agreement within 0.1% error between the finite element analysis and linear elastic deformation theory in the previous study. The amplified displacement, v_{amp} , is calculated from the geometric condition of the beam if the actuator displacement is X .

$$v_{amp} = l_{m1} \cdot \sin i_m \approx \frac{3}{4} \frac{l_{m1}}{l_{m2}} X = \alpha X. \quad (2)$$

The amplification factor of the system, α , is 20.06 in the design and 19.97 in the calculation from the measured dimension of the beam. In this experiment, the moving distance at the end of the long-cantilevers was monitored by an optical microscope (Olympus Co., SZX12) with an objective lens with a 50-times magnification coupled to a charge coupled device (CCD) camera (Hitachi, KP-F120CL). The resolution of the CCD was 6.45 $\mu\text{m}/\text{pixel}$ with 1392 \times 1040 pixels. The maximum frame rate was 30 fps. A block matching and linear compensation method was used for the image analysis [23, 25], which provided a 25 times greater resolution than that of the CCD. Consequently, the total resolution in the displacement of the system reached approximately 0.65 nm in theory.

The EANAT was fabricated from a silicon-on-insulator wafer with a thermal oxidized 5 μm thick active layer on 1 μm thick buried oxide (BOX) layer and a 525 μm thick silicon substrate. A conventional doping process was performed at the actuator and displacement sensor regions on the active layer. The device was fabricated by photolithography and a subsequent reactive ion etching process with inductive coupled plasma. The vaporized hydrofluoric acid (HF) etched the BOX layer to release the active layer from the substrate. Finally, the specimen part was coated with an Au film using a stencil mask method.

The new EANAT was smaller than the previously proposed devices; therefore, 16 devices were simultaneously fabricated on a 15 \times 15 mm^2 chip for sequential testing. The scanning electron microscopy (SEM) images of the EANAT

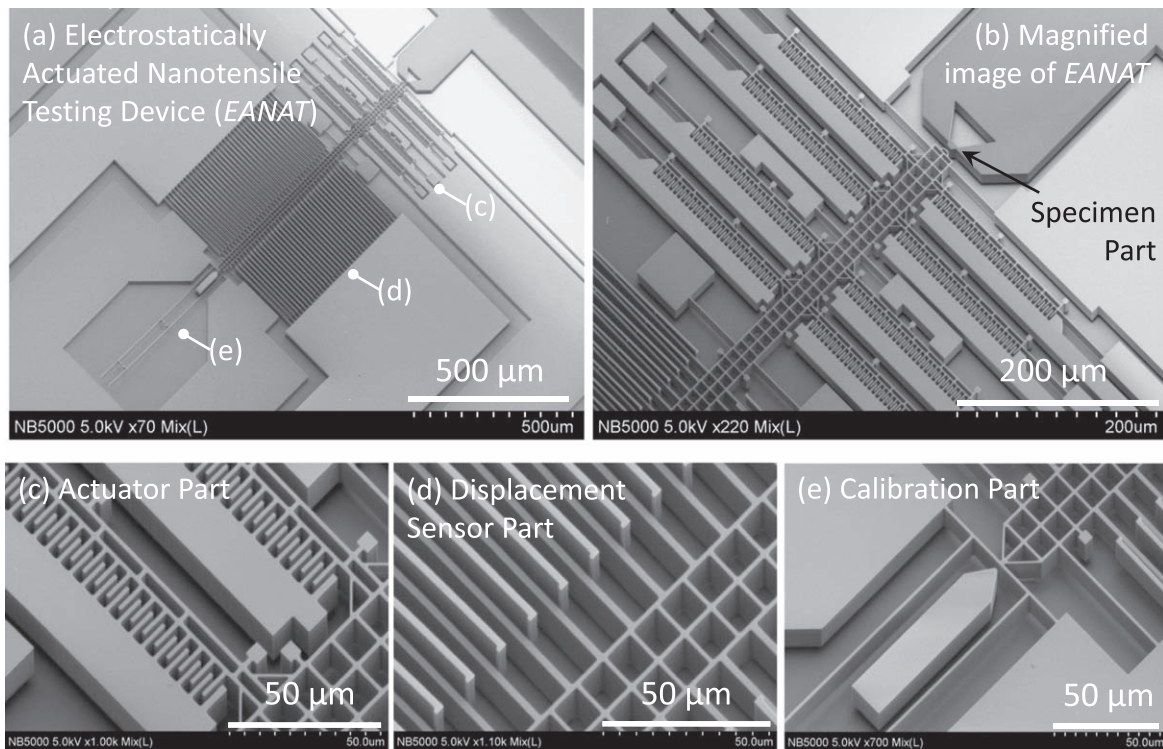


Figure 2. SEM images of the EANAT: (a) overall image of the EANAT and the magnified images of (b) the specimen, (c) electrostatic actuator, (d) differential displacement sensor, and (e) calibration part with the geometrical amplification system. The EANAT was fabricated by a conventional MEMS process.

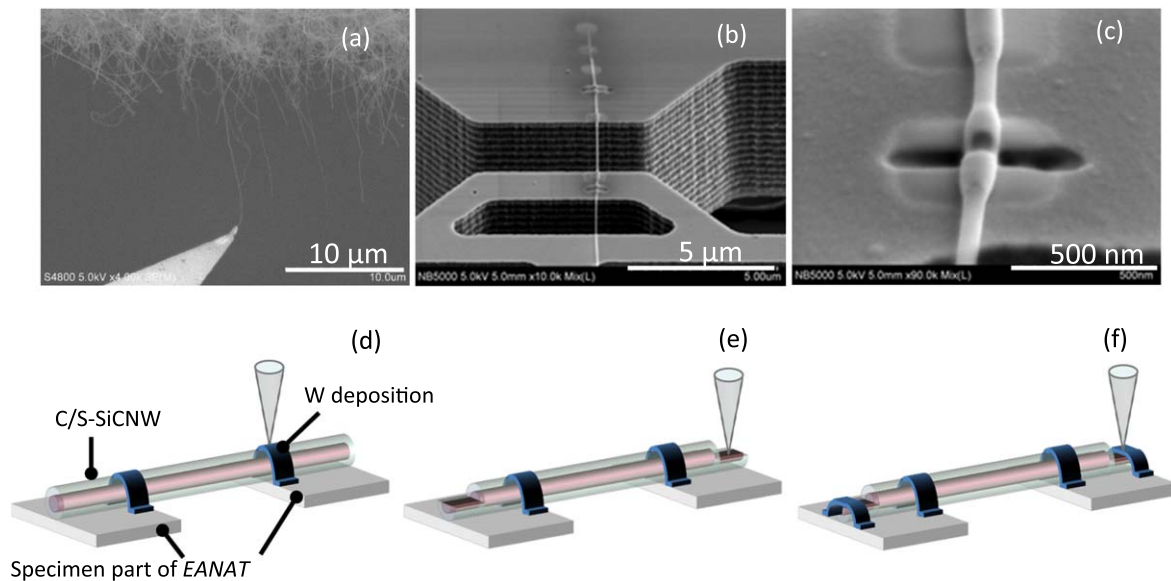


Figure 3. SEM images and schematics of the *in situ* SEM manipulation and bridging processes for the SiCNW on the EANATs: (a) extracting a C/S-SiCNW from the substrate used in the VLS growth by *in situ* SEM manipulation, (b) bridging the C/S-SiCNW at the gap of the specimen on the EANAT and temporarily fixing it by EBID, and (c) exposing the SiC core by the FIB. The further fixing process of an individual C/S-SiCNW is shown in the schematics of (d) FIB-assisted tungsten deposition, (e) exposing the SiC core by the FIB, and (f) making an electrical connection between the core and electrode pads.

are shown in figures 2(a)–(e). The electrostatically driven actuator (see figure 2(c)), parallel plate-type displacement sensor (see figure 2(d)), and calibration beams (see figure 2(e)) were successfully fabricated according to the device design.

2.3. Experimental methodology of the nanotensile test

Figures 3(a)–(f) show the SEM images and schematics of the bridging and electrical connecting processes of the C/S-SiCNW on the EANAT. The *in situ* SEM probe nanomanipulation system, including two probe stages and one sample

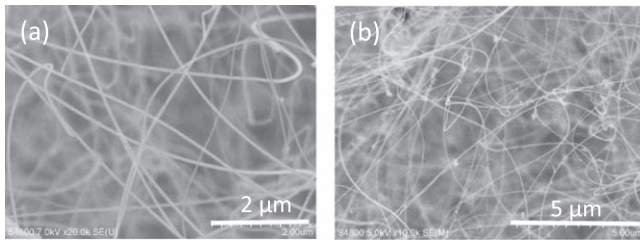


Figure 4. SEM images of the SiCNWs grown on the substrate: (a) ultra-long C/S-SiCNWs and (b) SiC cores after removing the SiO_x shell by the VHF process.

stage [26], was employed for picking up an individual nanowire from a substrate to fix it to the device. The probe approached below the free end of the C/S-SiCNW on the substrate, and the nanowire was fixed on the probe by electron beam induced carbon-based-contamination deposition (EBID) (see figure 3(a)). After removing the C/S-SiCNW from the substrate, the nanowire was moved to the specimen part of the EANAT and was temporarily attached to the device by EBID (see figure 3(b)). Next, the EANAT was replaced into the focused ion beam (FIB, Hitachi NB5000) in order to ensure the fixing and electrical connection of the nanowire. FIB-assisted tungsten (W) deposition was carried out for mechanically fixing the C/S-SiCNW (see figure 3(d)), and then, the SiO_x shell was etched by the FIB to expose the SiC core (see figure 3(e)). Finally, FIB-assisted W deposition was again performed to ensure an electrical connection between the SiC core and Au-coated specimen part of the EANAT (see figures 3(c) and (f)).

In the tensile test using the EANAT, the force, F , generated by the electrostatic actuator deflected the suspension beams on the device with a total stiffness of K_a , K_s , and K_b , and pulled an individually bridged nanowire with a stiffness of K_{NW} , as shown in figure 1(a). Thus, the tensile force from stretching the nanowire, P , is expressed by the following equation [25]:

$$P = (K_a + K_s + K_b)(X^{after} - X^{before}). \quad (3)$$

The parameter X^{before} is the displacement produced by the actuator before the failure of the nanowire, and X^{after} is that without the nanowire after the failure. In this study, the displacement was measured by monitoring the amplified cantilever at the calibration part, without using the capacitive sensors because of a small signal-to-noise ratio of the output voltage through the charge amplifier. The stiffness of each suspension beam was derived from the measured dimensions and Young's modulus of the beam, considering the non-linearity of stiffness owing to a large deformation [25].

3. Morphological characteristics of the core-shell SiCNWs

Figures 4(a) and (b) show the SEM images of grown C/S-SiCNWs and SiC cores prepared by removing the SiO_x shell from the C/S-SiCNWs with vaporized HF (VHF). The morphological characterization of the grown C/S-SiCNWs

revealed dense networks of ultralong nanowires with a length up to 100 μm and a mean diameter of 55 nm (see figure 4(a)). The SiC core after VHF etching of the SiO_x shell had a mean diameter ranging from 20 to 30 nm. Some nanoparticles were observed at the surface of the SiC cores. This could be attributed to the reaction products associated with H₂SiF₆ (see figure 4(b)) [30], which were not released from the surface.

The TEM images of the grown C/S-SiCNW and SiC core without the SiO_x shell are shown in figures 5(a)–(c), and a schematic of the 3C structure for SiC is shown in figure 5(d). The crystalline core wrapped by an amorphous layer is shown in figures 5(a) and (b). The crystal structure of the core was identified as cubic with a lattice interval of approximately 2.59 Å along the growth direction, which is roughly consistent with the distance, 2.51 Å, between the {111} planes of 3C-SiC. The SEM images of the SiC core without the shell showed a similar crystal structure to that of the C/S-SiCNW, and the core was 3C-SiC with the ⟨111⟩ axis along the growth direction (see figure 5(c)). There was minimal SiO_x shell on the surface of the core other than the residue, as shown in figure 4(b).

Stacking faults along {111} were occasionally observed in the SiC core. Figures 6(a)–(f) show the TEM images of two types of stacking faults in the SiC core, and the schematics of the 2H- and 4H-polytypes owing to the faults induced by a Shockley partial dislocation. An atomic rectangular pattern of 2.51 Å × 4.96 Å was observed along the growth direction, with a lattice interval of 2.48 Å (see figures 6(a) and (b)). This was in good agreement with 2H-SiC, which was produced by a stacking fault owing to the partial dislocation in the ⟨112⟩ direction. The 2H-SiC showed the growth direction of ⟨111⟩. Compared with the schematic of 4H-SiC in figures 6(f), 4H-SiC induced by a double-Schockley stacking fault was observed although the atomistic images in figures 6(d) and (e) were not sharp, where 4H-SiC seemed to grow in the ⟨112⟩ direction.

Therefore, the SiC core of the C/S-SiCNWs was composed of 3C-SiC with the ⟨111⟩ axis along the growth direction; however, the stacking faults caused by the partial dislocation occasionally produced hexagonal polytypes, such as 2H-, 4H-, and 6H-SiC.

4. Results and discussions

4.1. Tensile testing results

Figure 7(a) shows the relationship between the tensile displacement and voltage applied to the actuator of the EANAT, obtained from the uniaxial tensile test for the 73.9 nm diameter C/S-SiCNW. The measured displacement plotted as the open circles indicates the tensile elongation of the nanowire before its failure, whereas the displacement indicated by the filled circles corresponds to the moving distance of the actuator after the failure of the nanowire. The sharp rise of displacement at a voltage greater than 80 V suggested a brittle fracture of the nanowire. The tensile force required to stretch the nanowire was calculated from the difference in the

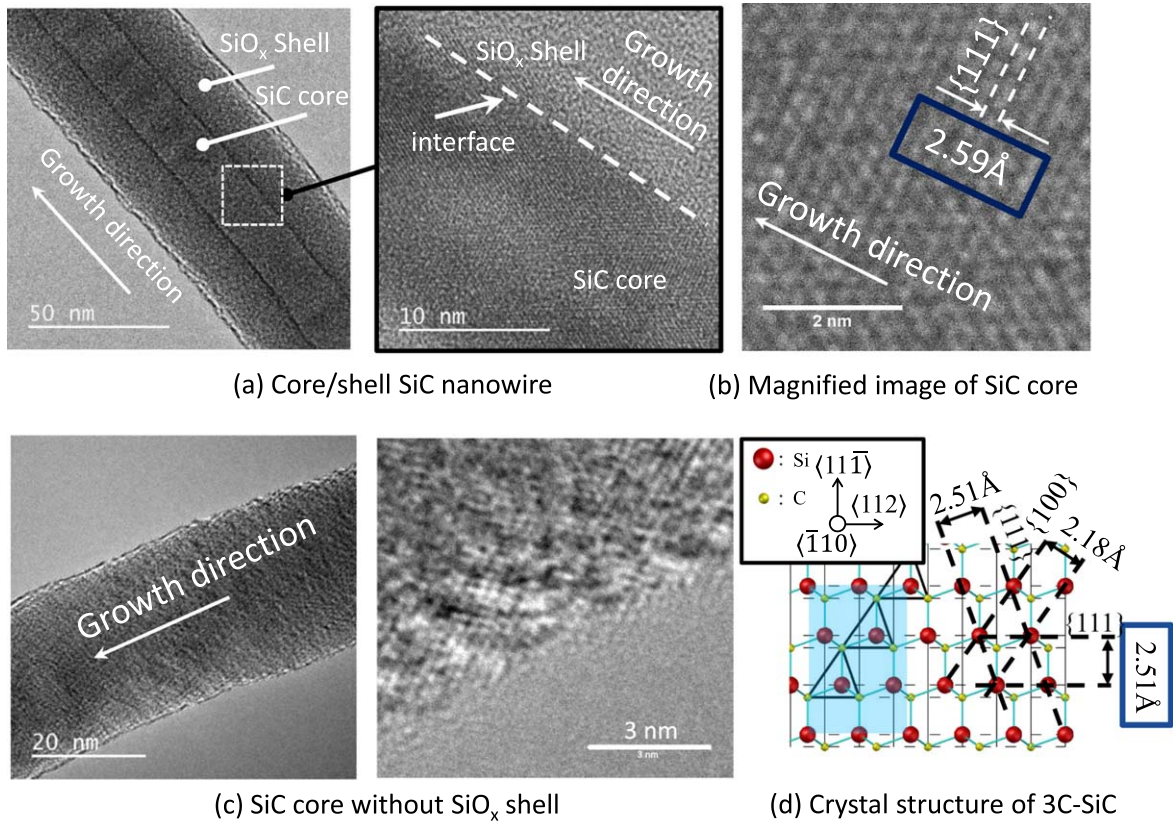


Figure 5. TEM images of the SiCNWs along with a schematic of the crystal structure in 3C-SiC: (a) C/S-SiCNW, (b) magnified image at the SiC core, (c) SiC core without the SiO_x shell, and (d) schematic of the crystal structure in 3C-SiC.

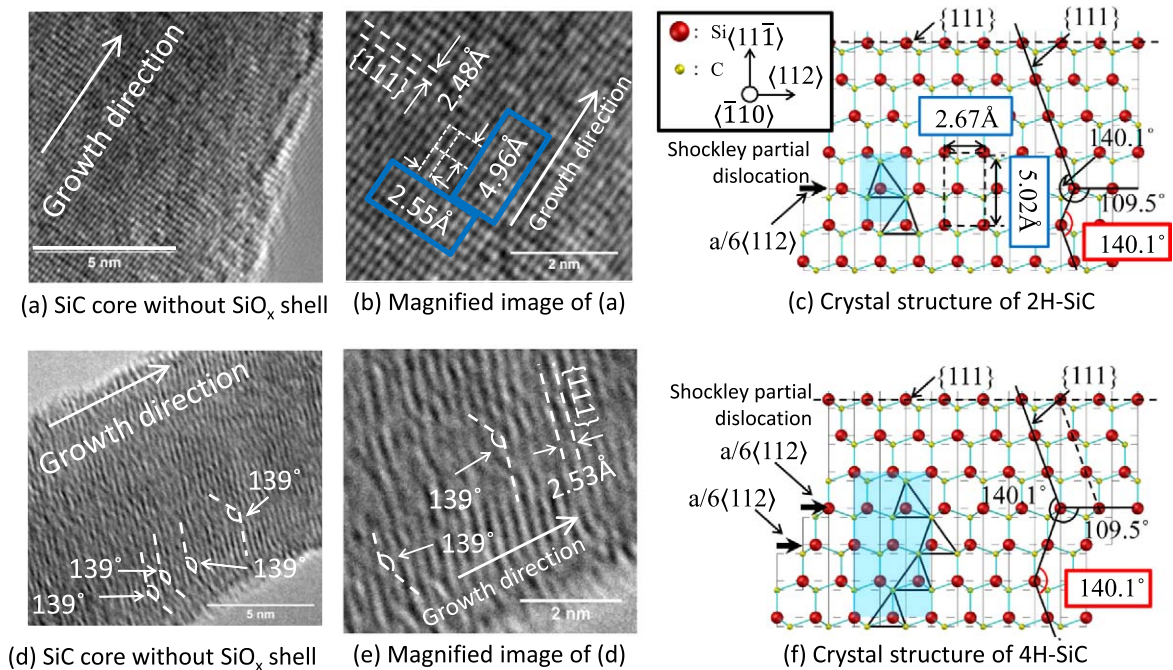


Figure 6. TEM images of the SiC cores along with a schematic of the crystal structure in 2H- and 4H-SiC: (a) SiC core without the SiO_x shell after removing the SiO_x shell by the VHF process, (b) magnified image of (a), (c) schematic of the crystal structure in 2H-SiC, (d) another SiC core without the SiO_x shell, (e) magnified image of (d), and (f) schematic of the crystal structure in 4H-SiC.

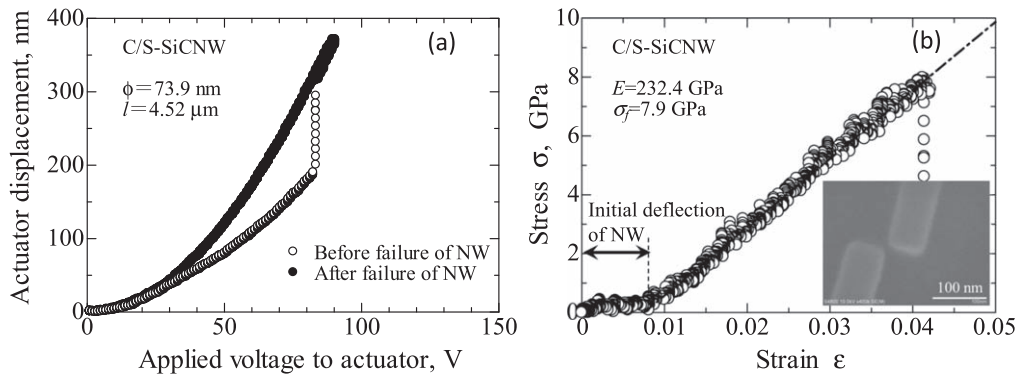


Figure 7. Tensile testing result for the C/S-SiCNW with a diameter of 73.9 nm and a length of 4.52 μm : (a) the relationship between the tensile displacement and the voltage applied to the actuator of the EANAT and (b) the stress–strain curve. The inserted SEM image in (b) shows the fracture point of the C/S-SiCNW.

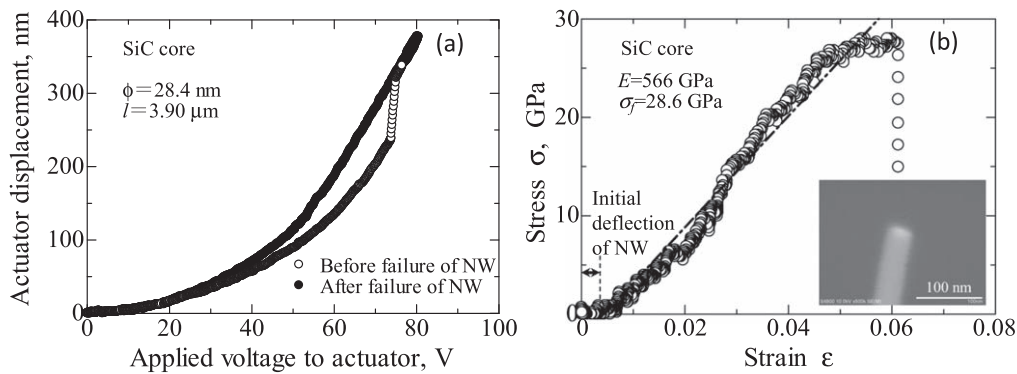


Figure 8. Tensile testing result for the SiC core with a diameter of 28.4 nm and a length of 3.90 μm : (a) the relationship between the tensile displacement and the voltage applied to the actuator of the EANAT and (b) the stress–strain curve. The inserted SEM image in (b) shows the fracture point of the SiC core.

displacement before and after the failure of the nanowire using equation (3); therefore, figure 7(a) could be converted to the tensile stress–strain relationship of the C/S-SiCNW, as shown in figure 7(b). The C/S-SiCNW showed a linear relationship between the stress and strain and a brittle fracture (see the inserted SEM image). Thus, the C/S-SiCNW indicated an elastic deformation behavior at room temperature. The Young's modulus and tensile strength of the nanowire were 232 GPa and 7.9 GPa, respectively.

Figures 8(a) and (b) show the tensile displacement with an increase of the applied voltage to the actuator and the stress–strain curve for the 28.4 nm diametric SiC core without the SiO_x shell, respectively. Although the measured displacement of the SiC core showed a similar trend to that of the C/S-SiCNW, the stress–strain curve showed nonlinearity, and the slope of the curve fluctuated. This could be attributed to the stacking faults at the high stress created during elastic deformation. The Young's modulus obtained from the linear approximation was 566 GPa, and the tensile strength was 28.6 GPa. These large values in the mechanical properties suggested that the SiC core could have a high crystallinity, which were in good agreement with previously reported values [31–33]. Table 1 lists the mechanical properties of the nanowires used in the tensile tests. The scatter of the data for the C/S-SiCNWs was smaller than that for the SiC cores.

4.2. Elastic properties of the core–shell SiCNWs and SiC cores

The Young's modulus values measured from the SiC cores showed a relatively large scatter. Therefore, this study has evaluated the validity of the experimental results. Here, the Young's modulus of the SiC cores was reverse calculated from the experimental data of the C/S-SiCNWs using the following equation:

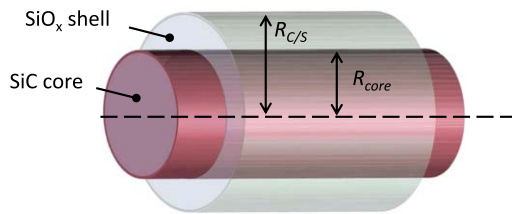
$$E_{\text{core+shell}} = (E_{\text{core}}R_{\text{core}}^2 + E_{\text{shell}}(R_{\text{C/S}}^2 - R_{\text{core}}^2))/R_{\text{C/S}}^2 \quad (4)$$

The parameter $E_{\text{core+shell}}$ is the Young's modulus of the C/S-SiCNW, and E_{shell} is the Young's modulus of the SiO_x shell. The parameter E_{core} is the Young's modulus of the SiC core, and $R_{\text{C/S}}$ is the radius of the C/S-SiCNW. The parameter R_{core} is the radius of the SiC core, as shown in figure 9.

The ratio of R_{core} to $R_{\text{C/S}}$ has been shown to be approximately 1.8 on average from TEM observations, although the TEM images were omitted here. The R_{core} predicted from the respective $R_{\text{C/S}}$ measured by the images are listed in table 2. If the Young's modulus of the SiO_x shell was assumed to be close to that of SiO_2 , 68 GPa [34], the Young's modulus of the SiC core was calculated to be in the range of 470–629 GPa, as listed in table 2. These values were close to the modulus of the tested SiC cores. Thus, this estimation suggested that the scatter in the Young's modulus of the SiC cores in the experiment was reasonable considering the data

Table 1. Summary of the mechanical properties with the dimensions for the C/S-SiCNWs and SiC cores used in the tensile tests. The dimensions of the nanowires are also listed.

Sample		Length (μm)	Diameter (nm)	Young's modulus E (GPa)	Fracture stress σ_f (GPa)
C/S-SiCNW	No.1	4.17	81.2	240	8.9
	No.2	4.52	73.9	232	7.9
	No.3	4.30	68.3	193	7.2
	No.4	3.95	93.0	193	6.8
	No.5	3.86	90.3	214	5.4
	Ave.	4.16	81.3	214	7.2
SiC core	No.1	3.90	28.4	566	28
	No.2	3.85	37.6	439	16
	Ave.	3.88	33.0	503	22

**Figure 9.** Schematic of the C/S-SiCNW for showing the dimensions of the core and shell.

of the C/S-SiCNWs; however, the cause of the scatter has been unknown yet.

In this study, on the assumption that the scatter of the Young's modulus for the SiC cores was affected by the stacking fault, the effect of the stacking fault on the Young's modulus of the SiC core was examined. Here, two types of 3C-SiC core models were proposed, including 4H-SiC based on the TEM observations, as shown in figures 10(a) and (b). Model A represented the stacking fault perpendicular to the growth direction of the $\langle 111 \rangle$ axis, and Model B represented the fault inclined at 19.4° to the $\langle 111 \rangle$ axis in theory. The Young's modulus of both models was calculated based on the volume ratio of the 4H-SiC to 3C-SiC core using the stiffness tensors of the 4H and 3C crystal structures [35, 36]. Figures 11(a) and (b) show the variations of the Young's modulus in the SiC core models with an increase of the volume ratio of 4H-SiC to 3C-SiC. The Young's modulus of Model A decreased from 603 to 538 GPa as the volume ratio of 4H-SiC increased, and this range in the modulus did not include the minimum value in the experiment (see figure 11(a)). In contrast, the Young's modulus estimated from Model B ranged from 603 to 425 GPa, including the experimental values. Therefore, the scatter of the Young's modulus for the SiC core could be attributed to the content of the stacking fault induced in the VLS growth, as one possibility.

4.3. I - V characteristics of the core-shell SiCNWs and SiC cores

The I - V characteristics for the C/S-SiCNW and SiC core listed in table 3 were measured under uniaxial tensile straining on the EANATs, as shown in figures 12(a) and (b). Both

nanowires showed a typical symmetric curve at each tensile strain, which is often observed in a general NW-based metal-semiconductor-metal (M-S-M) structure. This has been caused by a Schottky barrier junction at a metal-semiconductor contact point which plays a crucial role in the electrical transport in the M-S-M structure [37, 38]. Because the total voltage applied to the nanowires near a voltage of 0 V was mainly distributed on the two Schottky barriers, the slope of the curve near 0 V would be equivalent to the specific contact resistance, ρ_c , caused by the barrier junction. Therefore, ρ_c without straining was $0.074 \text{ M}\Omega \text{ cm}$ for the C/S-SiCNW and $0.22 \text{ M}\Omega \text{ cm}$ for the SiC core, which were obtained from the fitting slope in the range of $\pm 0.5 \text{ kV cm}^{-1}$.

Conversely, the electrical transport is dominated by the semiconducting nanowire at a large bias [38]. The electrical conductivity of the C/S-SiCNW without straining was estimated as $83.7 \mu\text{S cm}^{-1}$ at 55 kV cm^{-1} from the differential coefficient of the fitting function for the measured data plotted by closed circles, whereas that of the unstrained SiC core was $11.4 \mu\text{S cm}^{-1}$ at 50 kV cm^{-1} . The conductivity of the C/S-SiCNW was 7.5 times larger than that of the SiC core. This could have been caused by the fixed oxide charge of the SiO_x shell. According to the report by Seo *et al* [39], the effective carrier concentration in metal-catalyzed SiNWs is related to the polarity of the fixed oxide charge of their surrounding dielectric material, such as SiO_2 . Winkler *et al* [13] also reported similar results for VLS-grown SiNWs with unintentional p-type doping owing to the surface state and bulk impurities. SiO_2 as a dielectric via thermal oxidation surrounding the SiNW changed the transfer characteristic into an n-type because of the positive fixed oxide charges in the range of $Q_f = +10^{10} \text{ C m}^{-2}$ held by the SiO_2 shell. Thus, positive fixed oxide charges of the SiO_x shell in this study could have induced an accumulation regime of electrons at the SiO_x/SiC interface. Therefore, the current density of the C/S-SiCNW could be increased more than that of the SiC core without the SiO_x shell at each electric field regardless of the tensile strain.

The piezoresistivity of the VLS-grown C/S-SiCNWs behaved as an n-type semiconductor since the current density at each electric field increased with an increase of the tensile strain for both nanowires.

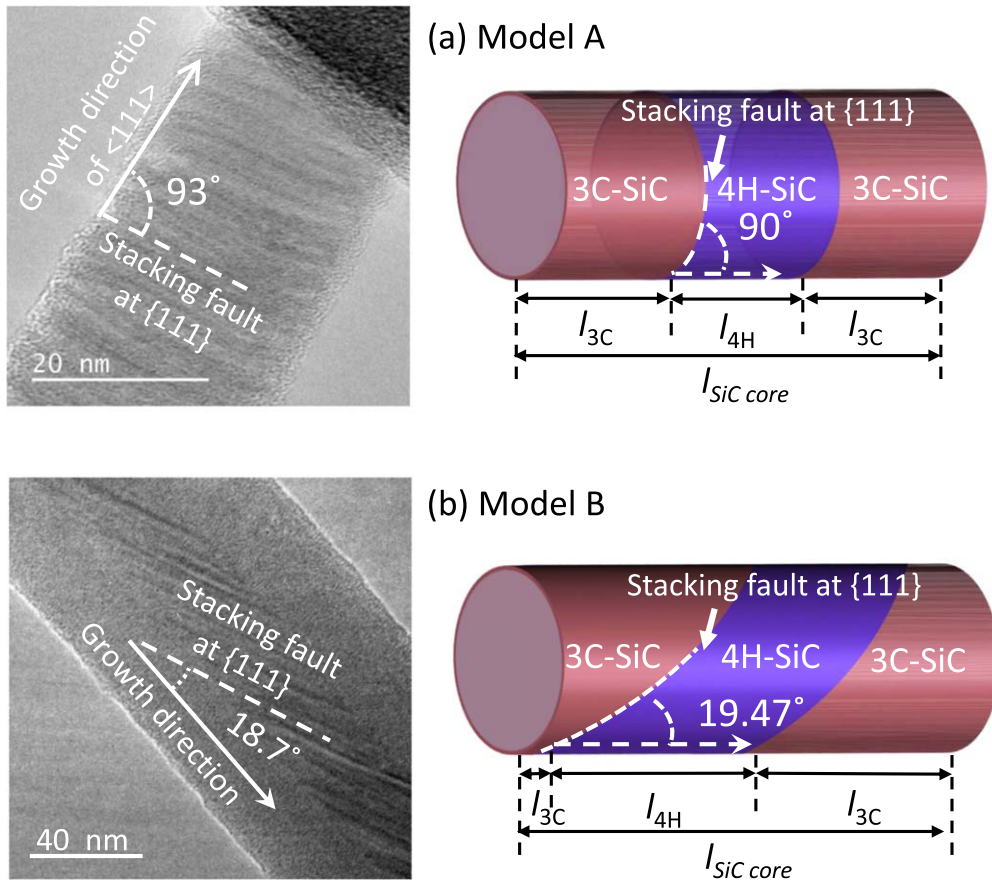


Figure 10. Schematics of the 3C-SiC core model, including 4H-SiC proposed based on the TEM observations: (a) Model A with the stacking fault perpendicular to the growth direction of the $\langle 111 \rangle$ axis and (b) Model B with that fault inclined at 19.4° to the $\langle 111 \rangle$ axis in theory.

Table 2. Young's modulus of the SiC core reversely calculated from the experimental data of the C/S-SiCNWs. R_{core} was predicted from $R_{C/S}$ measured by the TEM images.

Sample	Radius of C/S-SiCNW, $R_{C/S}$ (measured) (nm)	Thickness of SiO_x shell, R_{core} (predicted) (nm)	Young's modulus of SiC core, E_{core} (calculated) (GPa)
C/S-SiCNW No.1	40.8	22.7	629
No. 2	37.0	20.7	595
No. 3	34.1	19.1	470
No. 4	46.5	26.0	587
No. 5	45.2	25.2	537

4.4. Effect of the SiO_x shell on the piezoresistivity of the SiCNWs

Figures 13(a) and (b) show the variations of the resistance change ratio, $\delta\rho/\rho_{\varepsilon=0}$, with an increase of the tensile strain for the C/S-SiCNW and SiC core, respectively. The $\delta\rho/\rho_{\varepsilon=0}$ of both nanowires were nearly 0 owing to the initial deflection of the nanowires at the beginning of tensile straining; however, it decreased with an increase of the tensile strain as an n-type semiconductor. The $\delta\rho/\rho_{\varepsilon=0}$ of the C/S-SiCNW linearly decreased until 0.01ε , while that of the SiC core decreased until 0.03ε . In a larger strain range greater than 0.01ε in the C/S-SiCNW, the $\delta\rho/\rho_{\varepsilon=0}$ showed a reduction of the changing rate. The gauge factor of the C/S-SiCNW was estimated to be -31.8 at 0.005ε from the differential slope of the fitting

curve; however, it decreased to -13.2 at 0.02ε and -7.0 at 0.03ε . In contrast, the gauge factor of the SiC core was -13.6 at 0.01ε , and it decreased to -11.5 at 0.026ε . The large difference in the piezoresistive effect with and without the SiO_x shell was shown only at the low strain range less than 0.01ε , while the piezoresistive effect of both nanowires at the higher strain range demonstrated a similar trend.

These variations of the gauge factor could have been dominated by the strain induced modulation of the surface potential at a low strain level, and the strain induced band feature change at a high strain level. Winkler *et al* [13] demonstrated the influence of the surface potential of the SiNWs on their electrical resistivity under several uniaxial strains using gate-all-around FET-type three-point bending

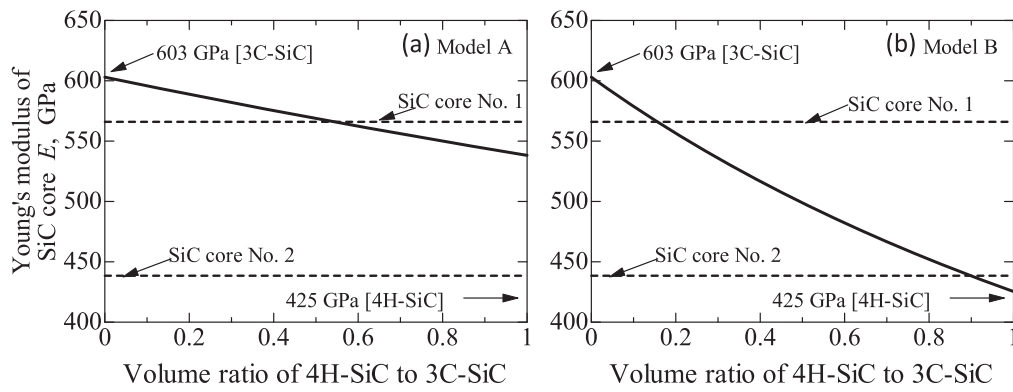


Figure 11. Variations of the Young's modulus in the SiC core models, calculated based on the stiffness tensors of the 4H and 3C crystal structures [33, 34], with an increase of the volume ratio of the 4H-SiC to 3C-SiC structures: (a) calculations using Model A and (b) calculations using Model B. The dashed lines in the figures show the maximum and minimum values obtained in the tensile tests of the SiC core without the SiO_x shell.

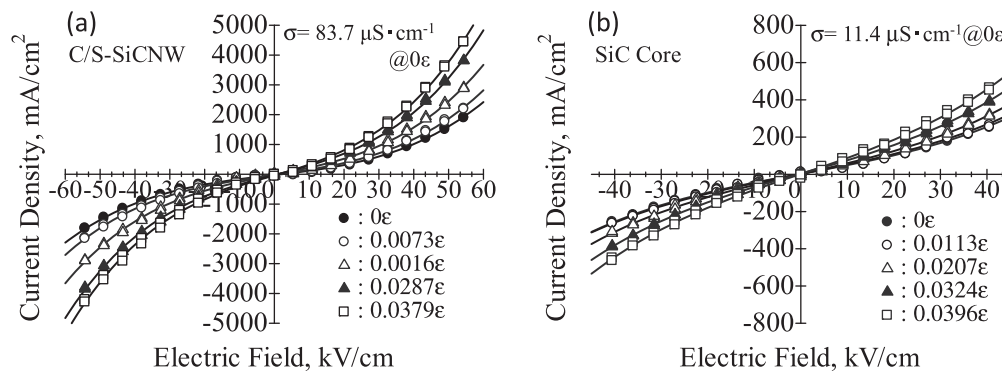


Figure 12. I - V curves measured under uniaxial tensile straining on the EANATs: (a) for the C/S-SiCNW and (b) for the SiC core without the SiO_x shell. The electrical conductivity of the C/S-SiCNW at 0ϵ was $83.7 \mu\text{S}\cdot\text{cm}^{-1}$ at $55 \text{ kV}\cdot\text{cm}^{-1}$, and that of the SiC core at 0ϵ was $11.4 \mu\text{S}\cdot\text{cm}^{-1}$ at $50 \text{ kV}\cdot\text{cm}^{-1}$.

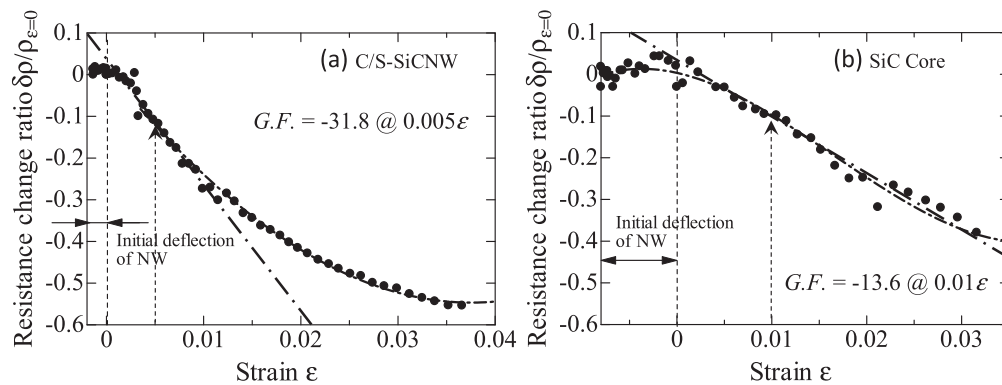


Figure 13. Variations of the resistance change ratio, $\delta\rho/\rho_{\epsilon=0}$, with an increase of the tensile strain: (a) for the C/S-SiCNW and (b) for the SiC core without the SiO_x shell. The maximum gauge factors were -31.8 at 0.005ϵ in the C/S-SiCNW and -13.6 at 0.01ϵ in the SiC core.

Table 3. Dimensions of the nanowires used in the I - V measurements.

Sample	Length l (μm)	Diameter of NWs ϕ (nm)	Diameter of core ϕ_{core} (nm)
C/S-SiCNW	3.68	68.4	38.2 (predicted)
SiC Core	4.44	—	45.8 (measured)

test devices with monolithically integrated VLS-grown SiNWs. They concluded that the carrier mobility of the VLS-grown SiNWs was determined by the filling or depopulation of the surface states owing to the strain-induced modulation of the surface potential at a low strain level, whereas at a high strain level, the narrowing strain induced bandgap and change of the band structural feature had a large influence on the carrier mobility in the SiNWs under straining [40–45].

Based on the above results, this study also could conclude that the positive fixed oxide charges of the SiO_x shell could have induced an accumulation layer of carrier electrons at the interface of the SiO_x/SiC core of the C/S-SiCNW, and this resulted in the large current density and large gauge factor of the C/S-SiCNW at a low strain. Thus, the large gauge factor of the C/S-SiCNW did not result from the giant piezoresistance effect of the one-dimensional semi-conductive nanowire. The change of the band structural feature of the SiCNWs could have determined the piezoresistivity at a high strain level, as well as that of the bulk SiC.

5. Conclusions

The mechanical and electrical properties of the VLS-grown SiCNWs with and without the SiO_x shell, with diameters ranging of 28 to 93 nm, were evaluated under uniaxial tensile loading using newly designed EANATs. The morphological characterization of the SiCNWs by TEM showed that they contained a 3C-SiC core with a $\langle 111 \rangle$ axis along the growth direction wrapped by an amorphous SiO_x shell. However, the stacking faults owing to the partial dislocation occasionally produced hexagonal polytypes, such as 2H-, 4H-, and 6H-SiC.

The tensile load of the nanowires was estimated from the total spring constant of the suspended beams, and the displacement of the nanowires was measured from the deflection of the geometric amplification system integrated on the EANATs. The C/S-SiCNWs were elastically deformed at room temperature. The Young's modulus and tensile strength were 214 GPa and 7.2 GPa for the C/S-SiCNWs and 503 GPa and 22 GPa for the SiC cores, respectively, on average. The validity of the Young's modulus obtained in the experiment was based on the dimensional ratio of the core to the shell or the stacking fault of the SiC core.

The VLS-grown C/S-SiCNWs behaved as an n-type semiconductor. The current density of the C/S-SiCNW without straining was higher than that of the SiC core because of the positive fixed oxide charges of the SiO_x shell, which could lead to the accumulation layer of carrier electrons at the interface of the SiO_x/SiC core. Thus, the gauge factor of $-32 @ 0.005 \varepsilon$ for the C/S-SiCNW was 2.3 times larger than that of the SiC core at approximately 0.01ε . However, at a high strain level greater than 0.02ε , the gauge factor was approximately -10 for both nanowires because the factor was dominated by the change of the band structural feature of the SiC.

Acknowledgement

This work was supported by JSPS KAKENHI Grant Number JP18H01335.

ORCID iDs

Akio Uesugi  <https://orcid.org/0000-0002-7913-3679>

Alois Lugstein  <https://orcid.org/0000-0001-5693-4775>

Yoshitada Isono  <https://orcid.org/0000-0003-2370-3246>

References

- [1] Müller G, Krötz G and Niemann E 1994 SiC for sensors and high-temperature electronics *Sensors Actuators A* **43** 259–68
- [2] Shor J S, Goldstein D and Kurtz A D 1993 Characterization of n-type β -SiC as a piezoresistor *IEEE Trans. Electron Devices* **40** 1093–9
- [3] Eickhoff M, Möller H, Kroetz G, Berg J V and Ziermann R 1999 A high temperature pressure sensor prepared by selective deposition of cubic silicon carbide on SOI substrates *Sensors Actuators A* **74** 56–9
- [4] Phan H-P *et al* 2014 Piezoresistive effect of p-type single crystalline 3C-SiC thin film *IEEE Electron Device Lett.* **35** 399–401
- [5] Akiyama T, Briand D and de Rooij N F 2012 Design-dependent gauge factors of highly doped n-type 4H-SiC piezoresistors *J. Microelectromech. Microeng.* **22** 085034
- [6] Phan H-P, Dao D V, Nakamura K, Dimitrijević S and Nguyen N-T 2015 The piezoresistive effect of SiC for MEMS sensors at high temperatures: a review *J. Microelectromech. Syst.* **24** 1663–77
- [7] Takao H, Matsumoto Y, Seo H, Ishida M and Nakamura T 1996 Analysis and design considerations of three-dimensional vector accelerometer using SOI structure for wide temperature range *Sensors Actuators A* **55** 91–7
- [8] Cimalla V, Pezoldt J and Ambacher O 2007 Group III nitride and SiC based MEMS and NEMS: materials properties, technology and applications *J. Phys. D: Appl. Phys.* **40** 6386–434
- [9] Zorman C A, Fleischman A J, Dewa A S, Mehregany M, Jacob C, Nishino S and Pirouz P 1995 Epitaxial growth of 3C-SiC films on 4 in. diam (100) silicon wafers by atmospheric pressure chemical vapor deposition. diam (100) silicon wafers by atmospheric pressure chemical vapor deposition *J. Appl. Phys.* **78** 5136–8
- [10] Eickhoff M, Möller M, Kroetz G and Stutzmann M 2004 Piezoresistive properties of single crystalline, polycrystalline, and nanocrystalline n-type 3C-SiC *J. Appl. Phys.* **96** 2872–7
- [11] He R and Yang P 2006 Giant piezoresistance effect in silicon nanowires *Nat. Nanotechnol.* **1** 42–6
- [12] Rowe A C H 2008 Silicon nanowires feel the pinch *Nat. Nanotechnol.* **3** 311–2
- [13] Cao J X, Gong X G and Wu R Q 2007 Giant piezoresistance and its origin in Si(111) nanowires: first-principles calculations *Phys. Rev. B* **75** 233302
- [14] Lugstein A, Steinmair M, Steiger A, Kosina H and Bertagnolli E 2010 Anomalous piezoresistance effect in ultrastrained silicon nanowires *Nano Lett.* **10** 3204–8
- [15] Winkler K, Bertagnolli E and Lugstein A 2015 Origin of anomalous piezoresistive effects in VLS grown Si nanowires *Nano Lett.* **15** 1780–5
- [16] Pan Z *et al* 2000 Oriented silicon carbide nanowires: synthesis and field emission properties *Adv. Mater.* **12** 1186–90

- [17] Khan A and Jacob C 2014 Random and self-aligned growth of 3C-SiC nanorods via VLS-VS mechanism on the same silicon substrate *Mater. Lett.* **135** 103–6
- [18] Wei J, Li K, Chen J, Yuan H, He G and Yang C 2013 Synthesis and growth mechanism of SiC/SiO₂ nanochains heterostructure by catalyst-free chemical vapor deposition *J. Am. Ceram. Soc.* **96** 627–33
- [19] Wei J, Li X, Zhao L, Wang J, Su H and Hao L 2018 Nitrogen-doped SiC/SiO_x nanowire heterostructure synthesized by pyrolysis deposition of phthalocyanine derivative *Ceram. Int.* **44** 20375–9
- [20] Gao F, Zheng J, Wang M, Wei G and Yang W 2011 Piezoresistance behaviors of p-type 6H-SiC nanowires *Chem. Commun.* **47** 11993–5
- [21] Shao R, Zheng K, Zhang Y, Li Y, Zhang Z and Han X 2012 Piezoresistance behaviors of ultra-strained SiC nanowires *Appl. Phys. Lett.* **101** 233109
- [22] Eickhoff M and Stutzmann M 2004 Influence of crystal defects on the piezoresistive properties of 3C-SiC *J. Appl. Phys.* **96** 2878–88
- [23] Kiuchi M, Matsui S and Isono Y 2007 Mechanical characteristics of FIB deposited carbon nanowires using an electrostatic actuated nano tensile testing device *J. Microelectromech. Syst.* **16** 191–201
- [24] Kiuchi M, Matsui S and Isono Y 2008 The piezoresistance effect of FIB-deposited carbon nanowires under severe strain *J. Micromech. Microeng.* **18** 065011
- [25] Oh H-J, Kawase S, Hanasaki I and Isono Y 2014 Mechanical characterization of sub-100-nm-thick Au thin films by electrostatically actuated tensile testing with several strain rates *Japan. J. Appl. Phys.* **53** 027201
- [26] Oh H-J, Omori H, Sadakata M, Tsubokura I and Isono Y 2014 Characterization of interlayer sliding deformation for individual multiwalled carbon nanotubes using electrostatically actuated nanotensile testing device *J. Microelectromech. Syst.* **23** 944–54
- [27] Yamauchi K, Obata K, Nakata S, Sugano K, Yashiro K and Isono Y 2016 Electrical resistance characterization of strain-induced multiwalled carbon nanotubes using MEMS-based strain engineering device *Sensors Mater.* **28** 75–88
- [28] Negri M, Dhanabalan S C, Attolini G, Lagonegro P, Campanini M, Bosi M, Fabbri F and Salviati G 2015 Tuning the radial structure of core-shell silicon carbide nanowires *CrystEngComm* **17** 1258–63
- [29] Rossi F *et al* 2015 Porphyrin conjugated SiC/SiO_x nanowires for x-ray-excited photodynamic therapy *Sci. Rep.* **5** 7606
- [30] Thomsen S M 1951 Acidimetric titrations in the fluosilicic acid system *Anal. Chem.* **23** 973–5
- [31] Lambrecht W R L and Segall B 1991 Calculated elastic constants and deformation potentials of cubic SiC *Phys. Rev. B* **44** 3694–785
- [32] Tong L and Mehregany M 1992 Mechanical-properties of 3C-silicon carbide *Appl. Phys. Lett.* **60** 2992–4
- [33] Su C M, Wuttig M, Fekade A and Spencer M 1995 Elastic and anelastic properties of chemical-vapor-deposited epitaxial 3C-SiC *J. Appl. Phys.* **77** 5611–5
- [34] Namazu T and Isono Y 2003 Quasi-static bending test of nanoscale SiO₂ wire at intermediate temperatures using AFM-based technique *Sensors Actuators A* **104** 78–85
- [35] Petrovic J J, Molewski J V, Rohr D L and Gac F D 1985 Tensile mechanical properties of SiC whiskers *J. Mater. Sci.* **20** 1167–77
- [36] Kamitani K, Grimsditch M, Nipko J C, Loong C-K, Okada M and Kimura I 1997 The elastic constants of silicon carbide: a Brillouin-scattering study of 4H and 6H SiC single crystals *J. Appl. Phys.* **82** 3152–4
- [37] Zhang Z Y, Jin C H, Liang X L, Chen Q and Peng L-M 2006 Current-voltage characteristics and parameter retrieval of semiconducting nanowires *Appl. Phys. Lett.* **88** 073102
- [38] Sze S M, Coleman D J Jr and Loya A 1971 Current transport in metal-semiconductor-metal (MSM) structures *Solid-State Electron.* **14** 1209–18
- [39] Seo K, Sharma S, Yasseri A A, Stewart D R and Kamins T I 2006 Surface charge density of unpassivated and passivated metal-catalyzed silicon nanowires *Electrochem. Solid-State Lett.* **9** G69–72
- [40] Mungu J, Bluet J-M, Marty O, Bremond G, Mermoux M and Rouchon D 2012 Temperature dependence of the indirect bandgap in ultrathin strained silicon on insulator layer *Appl. Phys. Lett.* **100** 102107
- [41] Nakamura K, Isono Y and Toriyama T 2008 First-principle study on piezoresistance effect in silicon nanowires *Japan. J. Appl. Phys.* **47** 5132–8
- [42] Nakamura K, Isono Y, Toriyama T and Sugiyama S 2009 First-principles simulation on orientation dependence of piezoresistance properties in silicon nanowires *Japan. J. Appl. Phys.* **48** 06FG09
- [43] Fischetti M V and Laux S E 1996 Band structure, deformation potentials, and carrier mobility in strained Si, Ge, and SiGe alloys *J. Appl. Phys.* **80** 2234–52
- [44] Munguía J, Bremond G, Bluet J M, Hartmann J M and Mermoux M 2008 Strain dependence of indirect band gap for strained silicon on insulator wafers *Appl. Phys. Lett.* **93** 102101
- [45] Zh Karazhanov S, Davletova A and Ulyashin A 2008 Strain-induced modulation of band structure of silicon *J. Appl. Phys.* **104** 024501